Journal of Computational Physics 459 (2022) 111124

Contents lists available at ScienceDirect

Journal of Computational Physics

www.elsevier.com/locate/jcp

A conservative and consistent implicit Cartesian cut-cell method for moving geometries with reduced spurious pressure oscillations

Zhihua Xie [a,*], Pengzhi Lin [b], Thorsten Stoesser [c]

[a] School of Engineering, Cardiff University, Cardiff, CF24 3AA, UK
[b] State Key Laboratory of Hydraulics and Mountain River Engineering, Sichuan University, Chengdu, 610065, China
[c] Department of Civil, Environmental and Geomatic Engineering, University College London, London, WC1E 6BT, UK

ARTICLE INFO

Article history:
Received 14 September 2021
Received in revised form 1 March 2022
Accepted 2 March 2022
Available online 8 March 2022

Keywords:
Cartesian cut-cell method
Moving body problem
Pressure oscillation
Complex geometries
Three-dimensional

ABSTRACT

A conservative and consistent three-dimensional Cartesian cut-cell method is presented for reducing the spurious pressure oscillations often observed in moving body simulations in sharp-interface Cartesian grid methods. By analysing the potential sources of the oscillation in the cut-cell framework, an improved moving body algorithm is proposed for the cut-cell method for the temporal discontinuity of the solid volume change. Strict conservation of mass and momentum for both fluid and cut cells is enforced through pressure-velocity coupling to reduce local mass conservation errors. A consistent mass and momentum flux computation is employed in the finite volume method. In contrary to the commonly cut-cell methods, an implicit time integration scheme is employed in the present method, which prevents numerical instability without any additional small cut-cell treatment. The effectiveness of the present cut-cell method for reducing spurious pressure oscillations is demonstrated by simulating various two- and three-dimensional benchmark cases (in-line and transversely oscillating cylinder, oscillating and free-falling sphere), with good agreement with previous experimental measurements and other numerical methods available in the literature.

1. Introduction

In computational fluid dynamics, two- (2D) and three-dimensional (3D) fluid flow over moving complex geometries appear in many practical engineering applications, *e.g.* marine hydrodynamics, offshore renewable energy, and fluid-structure interaction problems. In contrary to deal with the complex geometries in boundary-fitted methods [1–3] which needs re-meshing, Cartesian grid methods have become a popular alternative to solve fluid flow in a fixed Cartesian grid for moving body problems, due to its simplicity for mesh generation and easy data structure management [4,5].

Despite significant progress has been made for Cartesian grid methods (see reviews for immersed boundary method (IBM) [6], immersed interface method (IIM) [7], and the Cartesian cut-cell method [8]), there exist spurious pressure oscillations for Cartesian grid methods for moving body problems, which are associated with local mass conservation [9]. In IBM, the forcing term is added to the momentum equations without strictly satisfying the continuity equation [4], which lead to

* Corresponding author.
E-mail address: zxie@cardiff.ac.uk (Z. Xie).

https://doi.org/10.1016/j.jcp.2022.111124

pressure oscillations. There have been only a few IBM studies [9–19] on this issue in the literature and several techniques have been proposed to improve pressure oscillations. For the diffuse-interface IBM [11–13], a smooth delta function is used to spread the force across several stencils so that the oscillations are reduced. For the sharp-interface IBM, flow reconstruction [10] and extrapolation technique [14] are proposed to reduce the oscillations. Through modifying the continuity equation via a mass source/sink function [15–19], the pressure oscillations can be improved. Seo and Mittal [9] combined the cut-cell approach for the continuity equation and IBM for the momentum equation, the local mass conservation errors are further reduced, which leads to improved pressure oscillations.

In contrary to IBM, the Cartesian cut-cell method is very attractive as it enforces strict conservation of mass and momentum at a discretised level, even near the immersed boundary. The Cartesian cut-cell method has been applied to moving body problems for single-phase [20–25], multiphase flows [26–30] and fluid-structure interaction [31–33]. A common problem for cut-cell methods is the small cut-cells generated near the solid boundary which lead to numerical instability if there is no special treatment for small cells [34], which make it challenging to apply in 3D flow problems, especially involving moving geometries. Schneiders et al. [23] found that there is spurious pressure oscillation for the cut-cell method with the cell merging technique [22] and a smooth discretisation operator coupled with the cut-cell method can reduce the pressure oscillations.

In the present study, motivated by the previous studies to reduce spurious pressure oscillations, we further analyse the source of pressure oscillations in the Cartesian cut-cell framework. A conservative and consistent mass and momentum flux computation is used to ensure strict conservation of mass and momentum, even for the cut-cells, which is different from most of the IBMs. In addition, an implicit time integration scheme is used for the governing equations without any additional small-cell treatment, which prevents the common instability problems in small cut-cells existing in the literature. In order to further reduce the local mass conservation error associated with our piecewise-liner cut-cell boundary construction [35] for curved geometries, a new moving body algorithm is proposed here to significantly improve the local mass conservation error to reduce the pressure oscillations without interpolations and modifying cut-cells with smooth functions.

The paper is organised as follows. The description of the mathematical formulation and analysis for the source of pressure oscillations are presented in Section 2. The numerical method and cut-cell discretisation are presented in Section 3. The improvement of the pressure oscillations of the present cut-cell method is demonstrated by a number of 2D and 3D moving body flow problems in Section 4. Conclusion and future work are finally discussed in Section 5.

2. Mathematical formulation and source of pressure oscillation

2.1. Governing equations

The governing equations considered are the non-dimensional unsteady incompressible Navier–Stokes equations, given as:

$$\nabla \cdot \boldsymbol{u} = 0, \tag{1}$$

$$\frac{\partial \boldsymbol{u}}{\partial t} + \nabla \cdot (\boldsymbol{u} \otimes \boldsymbol{u}) = -\nabla p + \frac{1}{Re}\nabla^2 \boldsymbol{u}, \tag{2}$$

where $\boldsymbol{u}$ is the non-dimensional velocity vector with components (u, v, w) in the streamwise (x), vertical (y) and spanwise (z) direction, t and p are the non-dimensional time and pressure, and Re is the Reynolds number.

2.2. Moving geometry algorithm

In order to simulate the moving geometries, mass and momentum conservation are enforced at the cut cells (which contains both the fluid and solid) as well as the fluid cells, and the original governing equations are revised as [35]:

$$\nabla \cdot \boldsymbol{u} = \frac{1}{V}\frac{\mathrm{d}V_{\mathrm{solid}}}{\mathrm{d}t} = \psi, \tag{3}$$

$$\frac{\partial \boldsymbol{u}}{\partial t} + \nabla \cdot (\boldsymbol{u} \otimes \boldsymbol{u}) = -\nabla p + \frac{1}{Re}\nabla^2 \boldsymbol{u} + \boldsymbol{u}\psi, \tag{4}$$

whereas V_{solid} is the solid volume inside a control volume V and ψ is the mass source/sink term for the continuity equation. In the present cut-cell method, the above same governing equations are employed for all the control volumes which include either the full or cut cells, whereas the term ψ is zero for fluid cells and has a different value for each cut-cell which is related to the location of the moving body and its intersection with the background stationary Cartesian grid. It is worth noting that for flow over a fixed geometry, $\psi = 0$ for both fluid and cut cells as there is no change of the solid volume with respect to the time.

2.3. Source of pressure oscillation

Several numerical methods have been developed in the past to reduce the spurious pressure oscillation for moving body problems and they can be classified based on the revised governing equations as shown in Table 1. It is noted that

Table 1
Comparison between Cartesian grid methods based on the mass source/sink term ψ and the momentum body force term F. $\boldsymbol{U}_B$ is the moving velocity for the solid body, $\boldsymbol{n}$ is the normal vector of the cell face with surface area A.

Method	Examples	ψ	F
IBM-diffuse interface with smooth function	[11–13]	0	F_{IBM}
IBM-sharp interface with extrapolation	[14]	0	F_{IBM}
IBM-sharp interface with mass source	[15–18]	$\frac{1}{V}\sum \boldsymbol{U}_B \cdot \boldsymbol{n}A$	F_{IBM}
IBM-sharp interface with cut-cell	[9]	$\frac{1}{V}\frac{\mathrm{d}V_{\mathrm{solid}}}{\mathrm{d}t}$	F_{IBM}
Partial cell treatment	[36]	$\nabla \cdot \boldsymbol{U}_B$	0
Cartesian cut-cell method	[35]	$\frac{1}{V}\frac{\mathrm{d}V_{\mathrm{solid}}}{\mathrm{d}t}$	$\boldsymbol{u}\psi$

only the forcing term F_{IBM} is applied for the momentum equations in immersed boundary methods, without satisfying the continuity equation [9]. Several techniques, such as using a diffuse-interface IBM with smooth delta functions [11–13] or sharp-interface IBM with extrapolation [14], are proposed to suppress the pressure oscillation. In addition, a modified mass source term has been added together with the forcing terms for IBM to improve the pressure oscillation. However, the main source of pressure oscillation (such as for pressure equation or pressure correction equation) is local mass conservation error [9], which is related to the geometrical conservation of the dead and fresh cells, and the local geometry of the immersed body represented by the background Cartesian grid (shown in Fig. 1). Thus both the cut-cell IBM [9] and the partial cell treatment method [36] are proposed to satisfy the local mass conservation for a cut-cell, which significantly reduces the spurious pressure oscillation. However, the cut-cell approach is not considered for the momentum equations in a consistent way. Recently, the Cartesian cut-cell method [35] is developed, in which the cut-cell discretisation is taken into account for both the continuity and momentum equations to improve the spurious pressure oscillation.

In order to further investigate the local mass conservation error, a moving body with velocity $\boldsymbol{U}_B = (U_B, V_B)$ is considered in a 2D Cartesian grid shown in Fig. 1, where the fluid mass change and solid change are clearly presented from one time step to the next time step. A θ function is introduced in the cut-cell method [35], which represents the actual fraction of the total volume and face area available to the flow. Its value is 1 for fluid cells and 0 for solid cells whereas $0 < \theta < 1$ for cut cells. It can be seen that the fresh and dead cells are considered through the local mass conservation via Eq. (3). However, when considering a curved geometry, the actual geometry of the body is slightly different from the cut-cell representation due to the piecewise-linear boundary construction in the Cartesian cut-cell method (shown in Fig. 1(b) and Fig. 1(c)). This might lead to local mass conservation errors due to the evaluation of the term $\frac{\mathrm{d}V_{\mathrm{solid}}}{\mathrm{d}t}$. Seo and Mittal [9] already discussed this term as geometrical difference and noted that the pressure oscillation error is proportional to the cell area (2D) or volume (3D), and inversely proportional to the time step size. Thus, the pressure oscillation is reduced when the mesh is refined or when a larger time step size is used.

It is worth noting that using a high-order cut-cell representation of the interface (rather than piecewise-linear boundary construction) could potentially improve the calculation for the term $\frac{\mathrm{d}V_{\mathrm{solid}}}{\mathrm{d}t}$. However, the temporal variation of the volume change might still be large and there might be a discontinuity to calculate the gradient. In the present study, we use a slightly different approach to calculate the mass/sink term ψ, which uses the integral form to transform the temporal volume variation to a continuous velocity field from the body motion. The more detailed cut-cell discretisation and the treatment for the dead and fresh cells are discussed in Section 3.

3. Numerical method

The numerical method used in this study is based on the Cartesian cut-cell method for two-phase flows with moving bodies described by [35], but with a different moving body treatment. We provide a very brief description of the method for the single-phase incompressible Navier-Stokes equations here and the detailed information can be found in the original paper [35].

3.1. Cartesian cut-cell method

The finite volume method is employed to discretise the governing equations because it enforces the conservation of mass and momentum at a discretised level. The staggered Cartesian grid is used in this study, which has the advantage of strong coupling between the velocity and the pressure. Fig. 2 shows an example of the problem setup and the variable arrangement in a 3D Cartesian grid with cut-cells together with the name of locations used in the discretisation, in which the pressure is stored at the cell centre and the velocities are located on the face centre of the control volume.

In this study, the complex geometry of a solid is represented by a general level set function $\varphi(x, y, z)$, in which the value $\varphi(x, y, z) > 0$ in the fluid domain and $\varphi(x, y, z) < 0$ inside the solid domain. The solid boundary is represented as a sharp piecewise linear interface when $\varphi(x, y, z) = 0$, and it is a straight line in 2D (Fig. 2(c)) and a sloping plane in 3D (Fig. 2(b)). For a full fluid cell, the cell volume is $\Omega = \iiint_\Omega \mathrm{d}\Omega = \Delta x \Delta y \Delta z$ and the area of the face A is similarly calculated, *e.g.*, the one of the east face A_{e} is $A_{\mathrm{e}} = \iint_{\mathrm{e}} \mathrm{d}S = \Delta y \Delta z$. For a cut-cell shown in Fig. 2(b), the cell volume and the area of the east face are obtained as $\theta_c \Delta x \Delta y \Delta z$ and $\theta_e \Delta y \Delta z$, respectively. For example, Fig. 2(c) shows the 2D cut surface for the back face

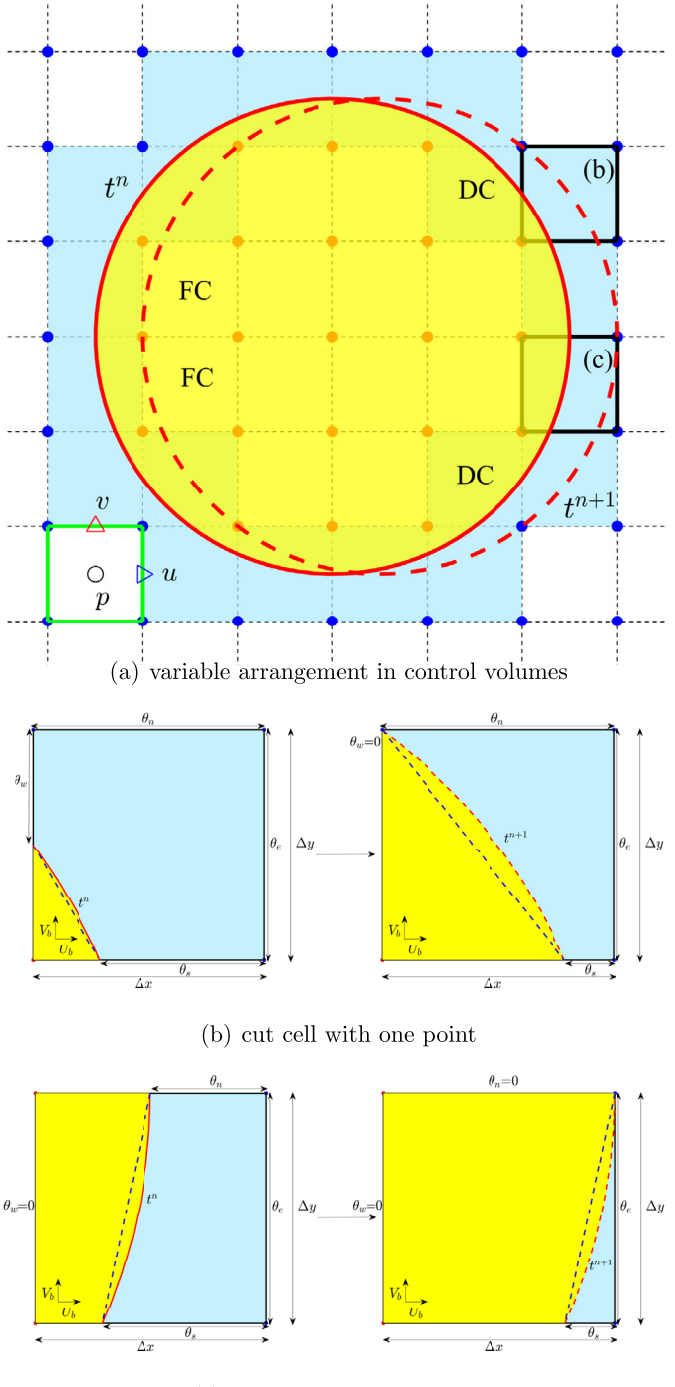

(a) variable arrangement in control volumes

(b) cut cell with one point

(c) cut cell with two points

Fig. 1. Moving body problem in a fixed Cartesian grid. (a) 2D computational setup and arrangement of variables (p, u, v), in which the velocities are stored on the face of the control volume and the pressure is stored at the centre of the control volume on a staggered Cartesian grid. The location of the moving boundary is shown at t^n and t^{n+1} time levels. Cut cells are shown in blue, where 'DC' and 'FC' represent the dead and fresh cells during one time step, respectively; (b) and (c) are two examples of a 2D cut-cell and the θ function change during one time step, with the yellow shaded area being solid. Red and blue lines are the actual geometry and the geometry represented by the cut-cell method. The subscripts e, w, n, and s denote the corresponding face of the control volume. Δx, and Δy are the grid spacing in the x, and y directions, respectively. (For interpretation of the colours in the figure(s), the reader is referred to the web version of this article.)

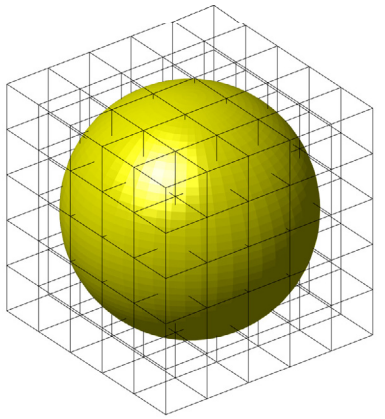

(a) problem

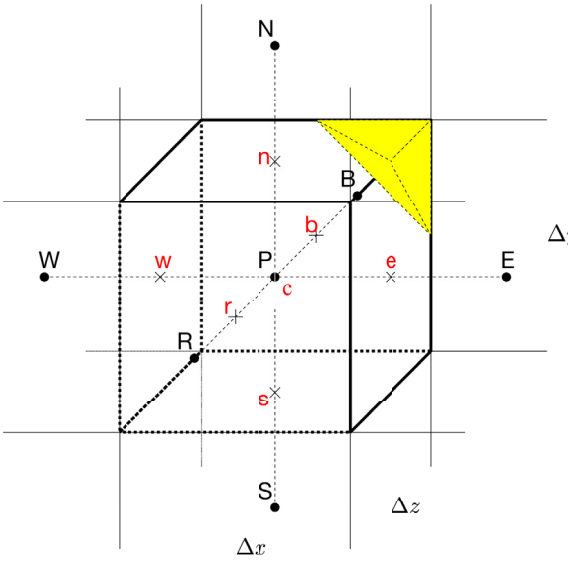

(b) 3D cut cell

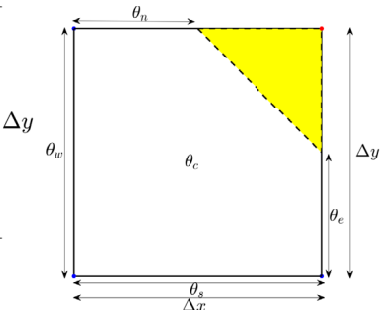

(c) 2D cut cell

Fig. 2. Schematic of a three-dimensional flow with a moving complex geometry: (a) 3D computational setup; (b) example of a 3D cut-cell with the yellow shaded area being solid. Name of the locations used in the discretisation is also shown, in which P is the present node, the upper-case letter E, W, N, S, B, and R denote neighbouring nodes on the east, west, north, south, back, and front with respect to the central node P. The lower-case e, w, n, s, b, and r denote the corresponding face of the control volume and c is the centre of the control volume. Δx, Δy, and Δz are the grid spacing in the x, y, and z directions, respectively; and (c) example of a 2D cut-cell on the back face of the control volume shown in (b).

of the 3D cut cell in Fig. 2(b). If the solid cuts from the middle of the edge on the north and east face, we can calculate the active cut edges as $\theta_w = \theta_s = 1$ and $\theta_n = \theta_e = 0.5$, and then the cut surface of the fluid area on the back face can be computed as $\theta_b = 7/8$. The area of the other faces can be calculated in a similar way and finally the cut volume can be obtained. More details about the 3D Cartesian cut-cell method can be found in [35].

3.2. Cut-cell treatment for the momentum equation

Considering a volume of fluid cell Ω which has an arbitrary domain, the surface of the control volume is S and the unit outward normal vector to the face f is $\boldsymbol{n}$. The momentum equation (Eq. (4)) can be recast into an integral formulation as below

$$\iiint_{\Omega} \frac{\partial \boldsymbol{u}}{\partial t} \mathrm{d}\Omega + \iint_{S} (\boldsymbol{u}\cdot\boldsymbol{n})\boldsymbol{u}\mathrm{d}S = \iiint_{\Omega} -\nabla p \mathrm{d}\Omega + \iint_{S} \frac{1}{Re}\frac{\partial \boldsymbol{u}}{\partial \boldsymbol{n}}\mathrm{d}S + \iiint_{\Omega} \boldsymbol{u}\psi \mathrm{d}\Omega. \tag{5}$$

A backward difference scheme is used for the time derivative term in Eq. (5), which leads to an implicit scheme for the Navier–Stokes equations for the latest time level $n+1$, such as the first-order backward Euler scheme as

$$\iiint_{\Omega} \frac{\partial \boldsymbol{u}}{\partial t} \mathrm{d}\Omega = \frac{\boldsymbol{u}^{n+1} - \boldsymbol{u}^{n}}{\Delta t} \theta_{\mathrm{c}} \Omega, \tag{6}$$

or the second-order backward Euler scheme as

$$\iiint_{\Omega} \frac{\partial \boldsymbol{u}}{\partial t} \mathrm{d}\Omega = \frac{3\boldsymbol{u}^{n+1} - 4\boldsymbol{u}^{n} + \boldsymbol{u}^{n-1}}{\Delta t} \theta_{\mathrm{c}} \Omega, \tag{7}$$

where Δt is the time step. For the implicit scheme, the θ function and flow variables are taken at the latest time level $n+1$ for the spatial discretisation as below. The solid fraction change during one time step Δt is considered in the source term ψ.

The finite volume discretisation of the advection term in Eq. (5) is obtained as

$$\iint_{S} (\boldsymbol{u} \cdot \boldsymbol{n}) \boldsymbol{u} \mathrm{d}S = \sum_{\mathrm{f}} m_{\mathrm{f}} \boldsymbol{u}_{\mathrm{f}}, \tag{8}$$

where $m = \boldsymbol{u} \cdot \boldsymbol{n} \theta A$ is the mass flux and the subscript f denotes the corresponding face of the control volume shown in Fig. 2(b).

The finite volume discretisation of the diffusion term in Eq. (5) for cut-cells is obtained as

$$\iint_{S} \frac{1}{Re} \frac{\partial \boldsymbol{u}}{\partial \boldsymbol{n}} \mathrm{d}S = \sum_{\mathrm{f}} \frac{1}{Re} \frac{\partial \boldsymbol{u}}{\partial \boldsymbol{n}} (\theta A)_{\mathrm{f}} + \tau_{\mathrm{w}} [(1-\theta) A]_{\mathrm{f}}, \tag{9}$$

where $\frac{\partial \boldsymbol{u}}{\partial \boldsymbol{n}}$ is calculated by the finite difference approach from the present point P to the neighbouring point nb as $\frac{\partial \boldsymbol{u}}{\partial \boldsymbol{n}} = \frac{\boldsymbol{u}_{\mathrm{nb}} - \boldsymbol{u}_{\mathrm{P}}}{\Delta_{\mathrm{Pnb}}}$ which is the nearest point normal to the faces of the 3D and 2D cut cells in Fig. 2(b and c), and τ_{w} is the wall shear stress on the face of the control volume.

The finite volume discretisation of the pressure gradient in Eq. (5) for cut-cells is obtained as

$$\iiint_{\Omega} -\nabla p \mathrm{d}\Omega = -\nabla p \theta_{\mathrm{c}} \Omega, \tag{10}$$

and the pressure gradient is calculated as

$$\nabla p = \left(\frac{p_{\mathrm{e}} - p_{\mathrm{w}}}{\Delta x}, \frac{p_{\mathrm{n}} - p_{\mathrm{s}}}{\Delta y}, \frac{p_{\mathrm{b}} - p_{\mathrm{r}}}{\Delta z}\right). \tag{11}$$

The finite volume discretisation of the source term in Eq. (5) for cut-cells is obtained as

$$\iiint_{\Omega} \boldsymbol{u} \psi \mathrm{d}\Omega = \boldsymbol{u} \psi \theta_{\mathrm{c}} \Omega. \tag{12}$$

3.3. Cut-cell treatment for the continuity equation

When dealing with the continuity equation, the exact conservation of mass is enforced to the discretised level in cut-cells. The continuity equation (Eq. (3)) can be recast into an integral formulation as below

$$\iint_{S} \boldsymbol{u} \cdot \boldsymbol{n} \mathrm{d}S = \iiint_{\Omega} \frac{1}{V} \frac{\mathrm{d}V_{\mathrm{solid}}}{\mathrm{d}t} \mathrm{d}\Omega. \tag{13}$$

Using divergence theorem on the right-hand-side term, the above equation can be rewritten as

$$\iint_{S} \boldsymbol{u} \cdot \boldsymbol{n} \mathrm{d}S = -\iint_{CC} \boldsymbol{U}_{B} \cdot \boldsymbol{n} \mathrm{d}S, \tag{14}$$

where $\boldsymbol{U}_{B}$ is the moving velocity vector of the solid body and CC is the solid surface for the cut cell.

The discretised form for the left-hand-side (LHS) of Eq. (14) in the control volume for the cut cell shown in Fig. 2(b) can be obtained as

$$\begin{aligned}\iint_S \boldsymbol{u}\cdot\boldsymbol{n}\mathrm{d}S &= \sum_{\mathrm{f}} \boldsymbol{u}_{\mathrm{f}}\cdot\boldsymbol{n}(\theta A)_{\mathrm{f}} \\ &= u_{\mathrm{e}}\theta_{\mathrm{e}}A_{\mathrm{e}} - u_{\mathrm{w}}\theta_{\mathrm{w}}A_{\mathrm{w}} + v_{\mathrm{n}}\theta_{\mathrm{n}}A_{\mathrm{n}} - v_{\mathrm{s}}\theta_{\mathrm{s}}A_{\mathrm{s}} + w_{\mathrm{b}}\theta_{\mathrm{b}}A_{\mathrm{b}} - w_{\mathrm{r}}\theta_{\mathrm{r}}A_{\mathrm{r}}.\end{aligned} \tag{15}$$

The right-hand-side (RHS) of Eq. (14) is the integration along the solid surface CC. As the area of each face can be calculated as $(1-\theta)A$, so the RHS can be obtained as

$$\begin{aligned}-\iint_{CC} \boldsymbol{U}_B\cdot\boldsymbol{n}\mathrm{d}S &= -\sum_{\mathrm{f}} \boldsymbol{U}_B\cdot\boldsymbol{n}[(1-\theta)A]_{\mathrm{f}} \\ &= -U_B(1-\theta_{\mathrm{e}})A_{\mathrm{e}} + U_B(1-\theta_{\mathrm{w}})A_{\mathrm{w}} \\ &\quad - V_B(1-\theta_{\mathrm{n}})A_{\mathrm{n}} + V_B(1-\theta_{\mathrm{s}})A_{\mathrm{s}} \\ &\quad - W_B(1-\theta_{\mathrm{b}})A_{\mathrm{b}} + W_B(1-\theta_{\mathrm{r}})A_{\mathrm{r}} \\ &= U_B\theta_{\mathrm{e}}A_{\mathrm{e}} - U_B\theta_{\mathrm{w}}A_{\mathrm{w}} + V_B\theta_{\mathrm{n}}A_{\mathrm{n}} - V_B\theta_{\mathrm{s}}A_{\mathrm{s}} + W_B\theta_{\mathrm{b}}A_{\mathrm{b}} - W_B\theta_{\mathrm{r}}A_{\mathrm{r}}.\end{aligned} \tag{16}$$

When substitute Eq. (15) and Eq. (16) into Eq. (14), the final discretised continuity equation is

$$\begin{aligned}&(u_{\mathrm{e}}-U_B)\theta_{\mathrm{e}}A_{\mathrm{e}} - (u_{\mathrm{w}}-U_B)\theta_{\mathrm{w}}A_{\mathrm{w}} + (v_{\mathrm{n}}-V_B)\theta_{\mathrm{n}}A_{\mathrm{n}} \\ &- (v_{\mathrm{s}}-V_B)\theta_{\mathrm{s}}A_{\mathrm{s}} + (w_{\mathrm{b}}-W_B)\theta_{\mathrm{b}}A_{\mathrm{b}} - (w_{\mathrm{r}}-W_B)\theta_{\mathrm{r}}A_{\mathrm{r}} = 0\end{aligned} \tag{17}$$

It can be seen that the cut-cell information for each control volume for their face areas is taken into account in the continuity equation to satisfy the divergence-free constraint at any time level. The volume change of the cut-cells (including fresh and dead cells) is also considered in a consistent way as used in the discretisation of the standard continuity equation, which is the key to reducing the pressure oscillation associated with the pressure correction equations as discussed in Section 3.4. It is worth noting that the final discretised continuity equation is equivalent to the partial cell treatment for the continuity equation used by Lin [36], although it is derived in a different way based on the finite difference method.

3.4. Navier-Stokes solver

The high-resolution scheme [37] is used for the advective flux. The second-order central difference scheme is used for diffusive flux, pressure gradient term and the pressure correction equations. It is worth noting that a consistent mass and momentum approach is used here for the staggered grid to discretise the nonlinear term, in which the mass flux $m_{\mathrm{f}} = \iint_S \boldsymbol{u}\cdot\boldsymbol{n}\mathrm{d}S$ for the momentum control volume is calculated based on the interpolation of the mass flux already available for the continuity equation [37]. Substituting all the discretised terms into Eq. (5) and subtracting the continuity equation multiplied by $\boldsymbol{u}_{\mathrm{P}}^{n+1}$, leads to

$$a_{\mathrm{P}}^{\boldsymbol{u}}\boldsymbol{u}_{\mathrm{P}}^{n+1} = \sum a_{\mathrm{nb}}^{\boldsymbol{u}}\boldsymbol{u}_{\mathrm{nb}}^{n+1} + b_{\mathrm{P}}^{\boldsymbol{u}} + A_{\mathrm{f}}(p_{\mathrm{P}} - p_{\mathrm{nb}}), \tag{18}$$

where $a^{\boldsymbol{u}}$ is the coefficient for the momentum equation, the subscripts P and $\mathrm{nb} = \mathrm{E, W, N, S, B, R}$ denote the variables in the present and neighbouring cells (shown in Fig. 2), respectively, and $b_{\mathrm{P}}^{\boldsymbol{u}}$ is the source term contained $\boldsymbol{u}^n$ and high-order terms due to the high-resolution scheme [38].

The PISO algorithm [39] is employed in this study for the pressure-velocity coupling and it is used to calculate the corrected pressure twice. For a guessed pressure distribution p^*, the discretised momentum equations can be solved to produce the fluid velocities $\boldsymbol{u}^*$, which satisfy the momentum equation (Eq. (18))

$$a_{\mathrm{P}}^{\boldsymbol{u}}\boldsymbol{u}_{\mathrm{f}}^{*} = \sum a_{\mathrm{nb}}^{\boldsymbol{u}}\boldsymbol{u}_{\mathrm{nb}}^{*} + b_{\mathrm{P}}^{\boldsymbol{u}} + A_{\mathrm{f}}(p_{\mathrm{P}}^{*} - p_{\mathrm{nb}}^{*}). \tag{19}$$

To obtain the pressure correction, the updated fluid velocities are substituted into the discretised continuity equation (Eq. (17)) and the resulting pressure correction equation has the following form

$$a_{\mathrm{P}}^{p}p_{\mathrm{P}}' = \sum a_{\mathrm{nb}}^{p}p_{\mathrm{nb}}' + b_{\mathrm{P}}', \tag{20}$$

where a^p is the coefficient for the continuity equation and the term b_{P}', called the mass residual, is the left-hand side of the discretised continuity equation (Eq. (17)) evaluated in terms of the fluid velocities $\boldsymbol{u}^*$.

A second correction step is introduced in the PISO algorithm [39] as

$$a_{\mathrm{P}}^{p}p_{\mathrm{P}}'' = \sum a_{\mathrm{nb}}^{p}p_{\mathrm{nb}}'' + b_{\mathrm{P}}'', \tag{21}$$

where the coefficients have the same value in the first pressure correction equation shown in Eq. (20) and the source term has been changed for calculating the mass residual based on the value of first velocity correction $\boldsymbol{u}'$.

Table 2
Comparison between boundary-fitted simulations, immersed boundary method, and the present study for flow past a fixed square cylinder at $Re = 100$.

Square cylinder at $Re = 100$	Method	$\bar{C}_D$	C_L^{rms}	St
Sohankar et al. [41]	boundary-fitted finite volume	1.477	0.156	0.146
Sen et al. [42]	boundary-fitted finite element	1.5287	0.1928	0.1452
Ryu and Iaccarino [43]	immersed boundary method	1.5642	0.1932	0.1506
Present study	Cartesian cut-cell	1.5385	0.2053	0.14

In this study, the algebraic equations are solved by the strongly implicit procedure method or Bi-CGSTAB (Bi-Conjugate Gradients Stabilized) method [40]. After solving the first and second pressure corrections (Eq. (20) and Eq. (21)), the solutions in a continuity control volume are updated as

$$\begin{aligned} p &= p^* + p' + p'', \\ \boldsymbol{u}_f &= \boldsymbol{u}_f^* + \boldsymbol{u}_f' + \boldsymbol{u}_f'', \end{aligned} \tag{22}$$

where

$$\begin{aligned} \boldsymbol{u}_f' &= \frac{A_f}{a_P^{\boldsymbol{u}}}(p_P' - p_{nb}'), \\ \boldsymbol{u}_f'' &= \frac{\sum a_{nb}^{\boldsymbol{u}} \boldsymbol{u}_{nb}' + A_f(p_P'' - p_{nb}'')}{a_P^{\boldsymbol{u}}}. \end{aligned} \tag{23}$$

3.5. Dead and fresh cells

It is worth noting that there is no special treatment in the present cut-cell method for the dead or fresh cells in moving body problems, which need some kind of interpolation in other methods. In the present cut-cell method, both the continuity and momentum equations are solved for all the full and cut cells ($\theta_c > 0$ shown in Fig. 1), which guarantee the conservation of mass and momentum locally as well as globally. For all the solid cells ($\theta_c = 0$), the velocity is specified as the moving body velocity $\boldsymbol{U}_B$. For the fresh cells ($\theta_c^n = 0$ and $\theta_c^{n+1} > 0$ during two time levels n and $n+1$ shown in Fig. 1), the new velocity for the fresh cells is obtained by solving the Navier–Stokes equations based on velocity value in the previous time level $\boldsymbol{u}^n = \boldsymbol{U}_B$; whereas for the dead cells, the new velocity is set to $\boldsymbol{u}^{n+1} = \boldsymbol{U}_B$ as the fluid volume becomes zero.

4. Results and discussion

In this section, we assess the accuracy and performance of this new approach. First, a benchmark case for the flow past a fixed square cylinder is studied to demonstrate the cut-cell method to deal with sharp-interface problems. Then the source of the pressure oscillation is discussed and a convergence study is performed for a standard benchmark to investigate the effects of grid and time-step sizes. Furthermore, two 2D test cases for an in-line and transversely oscillating circular cylinder are considered, in which the results are compared with experimental measurements and other numerical methods. After that, a 3D oscillating sphere is simulated to validate the present cut-cell treatment for 3D moving bodies. Finally, a single free-falling sphere is considered and its trajectory is compared with the experimental data, demonstrating the capability of the new cut-cell method in dealing with fluid-structure interaction problems.

4.1. Flow past a fixed square cylinder

The flow past a fixed square cylinder is considered first using the sharp-interface cut-cell method. The simulation for flow at $Re = 100$ is carried out in a large square domain ($[-20D, 40D] \times [-20D, 20D]$) with the square cylinder located at $(0, 0)$. A uniform velocity U is specified at the inlet whereas the zero gradient boundary condition is applied for other variables along the boundaries. A non-uniform Cartesian grid (300×264) is used to discretise the computational domain with uniform meshes $h = \Delta x_{min} = \Delta y_{min}$ ($h/D = 1/32$) in the vicinity of the square cylinder. A constant time step $\Delta t = 0.001 D/U$ is used in the simulation in order to minimise the temporal discretisation error.

An example of the snapshot for the streamlines and the corresponding vorticity field is shown in Fig. 3(a) and (b), respectively. It can be seen that a separation bubble is developed near the back face of the cylinder and the periodic vortex shedding is observed in the wake region. After the flow establishment, the time history of the drag C_D and lift C_L coefficients is presented in Fig. 3(c). The fluctuation of the lift is larger than that of the drag and the power spectrum from the lift is shown in Fig. 3(d), which demonstrates a single dominant peak frequency for the vortex shedding. The predicted mean drag coefficient, lift fluctuation and the Strouhal number are presented in Table 2 and compared with other boundary-fitted [41,42], immersed boundary [43] methods in the literature. A good agreement is obtained with the present method, demonstrating the capability of the cut-cell method to resolve sharp-interface geometries using a relatively coarse mesh.

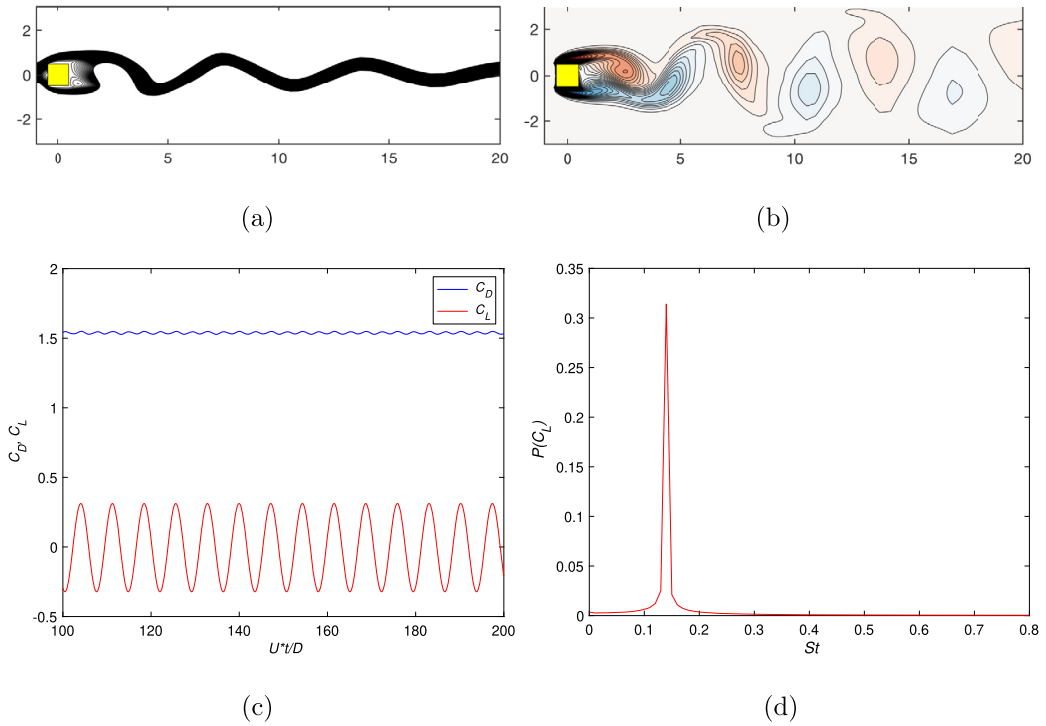

Fig. 3. Flow past a fixed square cylinder at $Re = 100$: (a) instantaneous streamlines; (b) instantaneous vorticity field; (c) time history of total drag C_D and lift C_L coefficients; and (d) the power spectrum of the lift signal in (c).

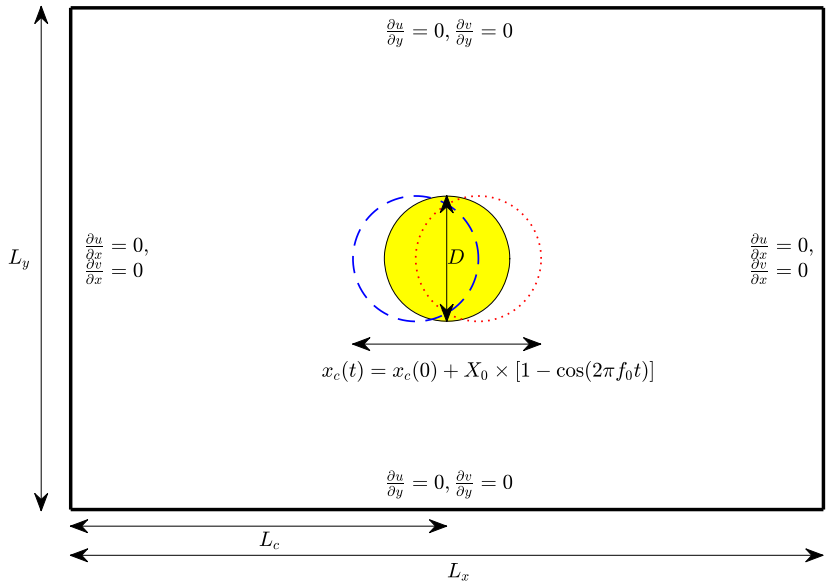

Fig. 4. Schematic of the computational setup for the oscillating circular cylinder problem, in which a circular cylinder of diameter D is oscillating horizontally in a quiescent fluid in a domain $L_x \times L_y$ with zero gradient boundary conditions for outer boundaries.

4.2. Source of pressure oscillation and convergence study: horizontally oscillating cylinder

In order to investigate the generation of spurious pressure oscillations in moving body problems, the test case proposed by Seo and Mittal [9] is considered here. Fig. 4 shows the computational setup, in which a circular cylinder of the diameter D with its centre located at (x_c, y_c), starts to oscillate sinusoidally in the x direction as

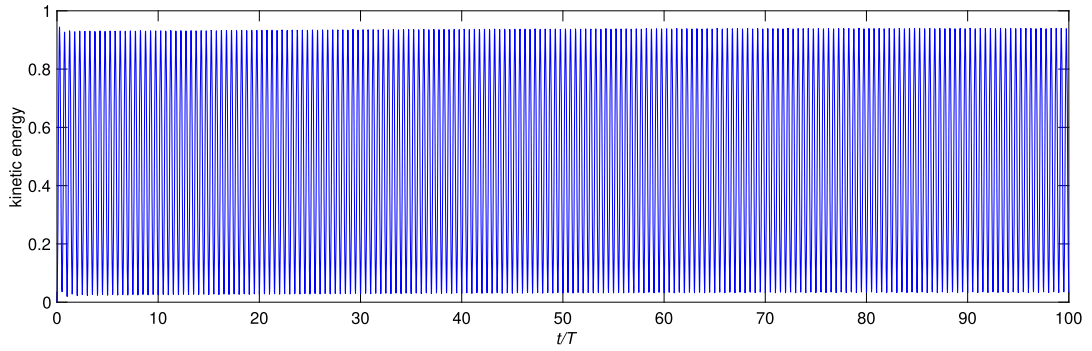

Fig. 5. Time history of the normalised kinetic energy predicted by the present method with mass and momentum conservation. The kinetic energy is calculated for the fluid in the whole domain and normalised by $\frac{1}{2}\rho A_{\text{cylinder}} U_0^2$.

$$
\begin{aligned}
x_c(t) &= x_c(0) + X_0[1 - \cos(2\pi f_0 t)], \\
u_c(t) &= U_0 \sin(2\pi f_0 t),
\end{aligned}
\tag{24}
$$

where $U_0 = 2\pi f_0 X_0$ is the maximum velocity, X_0 and $T = 1/f_0$ are the amplitude and period of oscillation, respectively. The Reynolds and Strouhal numbers are defined as $Re = U_0 D/\nu$ and $St = f_0 D/U_0$. The total pressure drag on the body is calculated as $C_{PD} = \frac{\int p(\boldsymbol{n}\cdot\boldsymbol{i})dS}{0.5\rho D^3 f_0^2}$.

We follow the same computational parameters used in [9], where $X_0 = 0.125D$, $Re = 78.5$ and $St = 1.27$. The simulations are carried out in a square domain ($[-2D, 2D] \times [-2D, 2D]$) with the cylinder located at the centre. Zero gradient boundary conditions are applied for the velocity and pressure at the outer boundaries.

First, in order to investigate the effect of conservation for the mass and momentum, three different scenarios are considered, namely: no mass and no momentum conservation (the mass source/sink term ψ is ignored); mass conservation and no momentum conservation (the ψ term is considered, but the cut-cell discretisation is ignored in the momentum equation); and mass and momentum conservation (the present method). All the simulations are performed on a uniform 64×64 grid with a fixed time step $\Delta t/T = 0.002$. In addition to the total pressure drag, the kinetic energy of the fluid in the whole domain is also taken into account, which is normalised by $\frac{1}{2}\rho A_{\text{cylinder}} U_0^2$. Fig. 5 shows an example of the kinetic energy predicted by the present method and it can be seen that periodic transformation of the kinetic energy is obtained from the simulation with good conservative property. In order to compare three different scenarios, the pressure drag coefficient and the kinetic energy for the last oscillation period are presented in Fig. 6. It can be observed that the flow field is not well captured when the mass conservation is not satisfied and there is a significant reduction for the momentum. When the mass conservation is enforced, there is little effect for the momentum conservation for the pressure drag, and the cut-cell discretisation for the Navier-Stokes equations produces better momentum conservation.

The simulations are also performed on a uniform 64×64 grid with a fixed time step $\Delta t/T = 0.002$ using the cut-cell method with the original moving body algorithm [35] and present moving body technique. The time histories of the total fluid mass conservation of the system, the integration of source term ψ for the whole domain, the pressure drag coefficient C_{PD} and the normalised kinetic energy are plotted in Fig. 7. It is worth noting that in order to gain insight into sources of spurious force oscillations, these quantities are shown at every time step in one oscillation period. The total fluid mass conservation error is very small (in the order of $O(10^{-5})$) for the coarse mesh used here. This is associated with the geometrical shape error to represent the circular shape of the cylinder using the cut-cell method and it will decrease when the mesh is refined. It can be seen that the present method significantly reduces the pressure oscillations although both methods predict a similar trend for the pressure drag. This is achieved by using the proposed new treatment for the solid volume change in the ψ term, which is much smoother and its fluctuation is at least one order smaller when compared to the original treatment. In addition, there is no oscillation for the kinetic energy and the present method has better conservation for the momentum. It is worth mentioning that this improvement is obtained by satisfying the fluid volume/mass conservation more accurately through the conservative and consistent cut-cell method around the moving body, without any force modification or interpolation of the flow field as used in IBM. This indicates that the mass conservation property for the cut cells is the major resource of spurious pressure oscillations for moving body problems.

In order to investigate the effect of grid size, four different uniform mesh resolutions (64^2, 128^2, 256^2, and 512^2 cells) are used in the simulation with a constant time step $\Delta t/T = 0.002$, in which the cylinder diameter D is covered by 16, 32, 64, and 128 cells, respectively. Fig. 8(a) shows the time histories of the pressure drag coefficient. It can be observed that smooth drag coefficients are obtained by the present method and there are only small oscillations when the cylinder passes the middle point where the velocity is maximum. The pressure oscillation is reduced when the mesh is refined, which is consistent with previous study [9]. This is mainly due to the decreased conservation error for the volume change term $\Delta V/\Delta t$ for the cut cells when refining the mesh for the fixed time step.

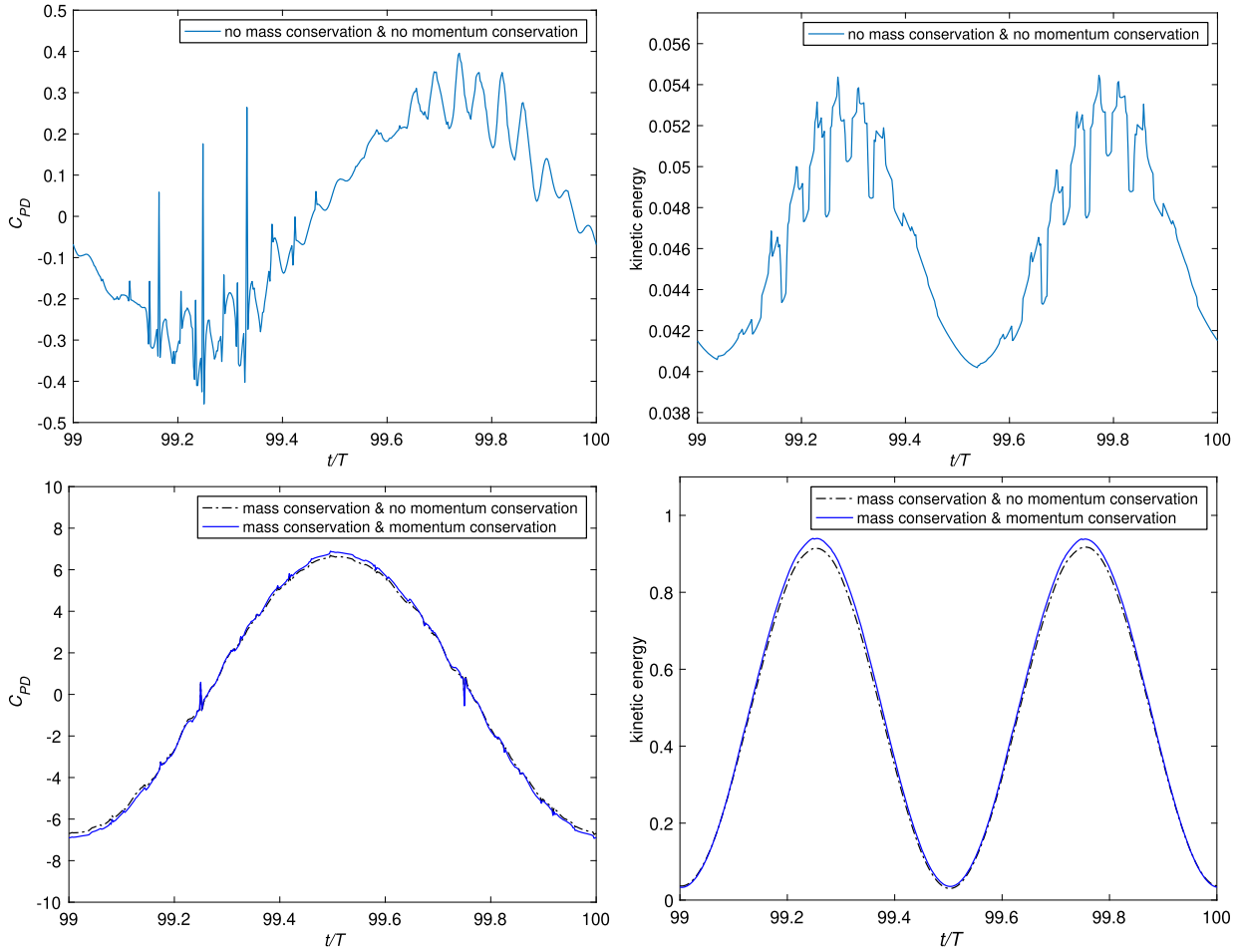

Fig. 6. Time histories of the pressure drag coefficient C_{PD} (left) and the normalised kinetic energy (right) for the horizontally oscillating circular cylinder in one period for the 64×64 mesh: comparison between different treatment for the conservation of mass and momentum.

In order to investigate the effect of time-step size, four different time steps with $\Delta t/T = 0.002, 0.004, 0.008, 0.016$ ($CFL = 0.025, 0.05, 0.1, 0.2$) are used for the grid (64×64 cells). Fig. 8(b) shows the time histories of the pressure drag coefficient plotted for every time step during the simulations. It can be seen that much smoother pressure variation is obtained for larger time-step size, which effectively decreases the conservation error when calculating the term $\Delta V/\Delta t$.

4.3. In-line oscillating circular cylinder in a fluid at rest

After obtaining reduced pressure oscillations, we start to validate the kinematics of the flow field for an in-line oscillating cylinder, which is very important in ocean and offshore engineering applications. The LDA experiment performed by [44] is studied here, which has been widely used as a benchmark case for other numerical methods [14,44]. The computational setup is similar to the previous case shown in Fig. 4 and details can be found in [44], where a cylinder is oscillating ($x_c(t) = x_c(0) - X_0 \sin(2\pi f_0 t)$) in a fluid at rest with a Reynolds number $Re = 100$ and a Keulegan-Carpenter number $KC = 5$, respectively. A larger computational domain ($[-30D, 30D] \times [-20D, 20D]$) is used in this case, with zero gradient boundary conditions being applied at outer boundaries. A non-uniform grid 1200×800 is used for spatial discretisation with uniform meshes $h = \Delta x_{\min} = \Delta y_{\min}$ ($h/D = 1/128$) in the vicinity of the cylinder. The CFL number is kept as constant 0.5 in the simulation.

It was shown in [44] that there is periodic vortex shedding in the vicinity of the oscillating cylinder. In order to make some quantitative comparisons with the experimental measurements, Fig. 9 shows the computed and measured velocity profiles (u and v) for three different phases during one oscillation period at four different streamwise locations x. The streamwise velocity u has a similar shape across the centre in the x axis while the vertical velocity v has a different sign with a similar profile. It can be seen that a good agreement is obtained between the simulation and experiment, which is similar to the body-fitted [44] and embedded-boundary [14] approaches.

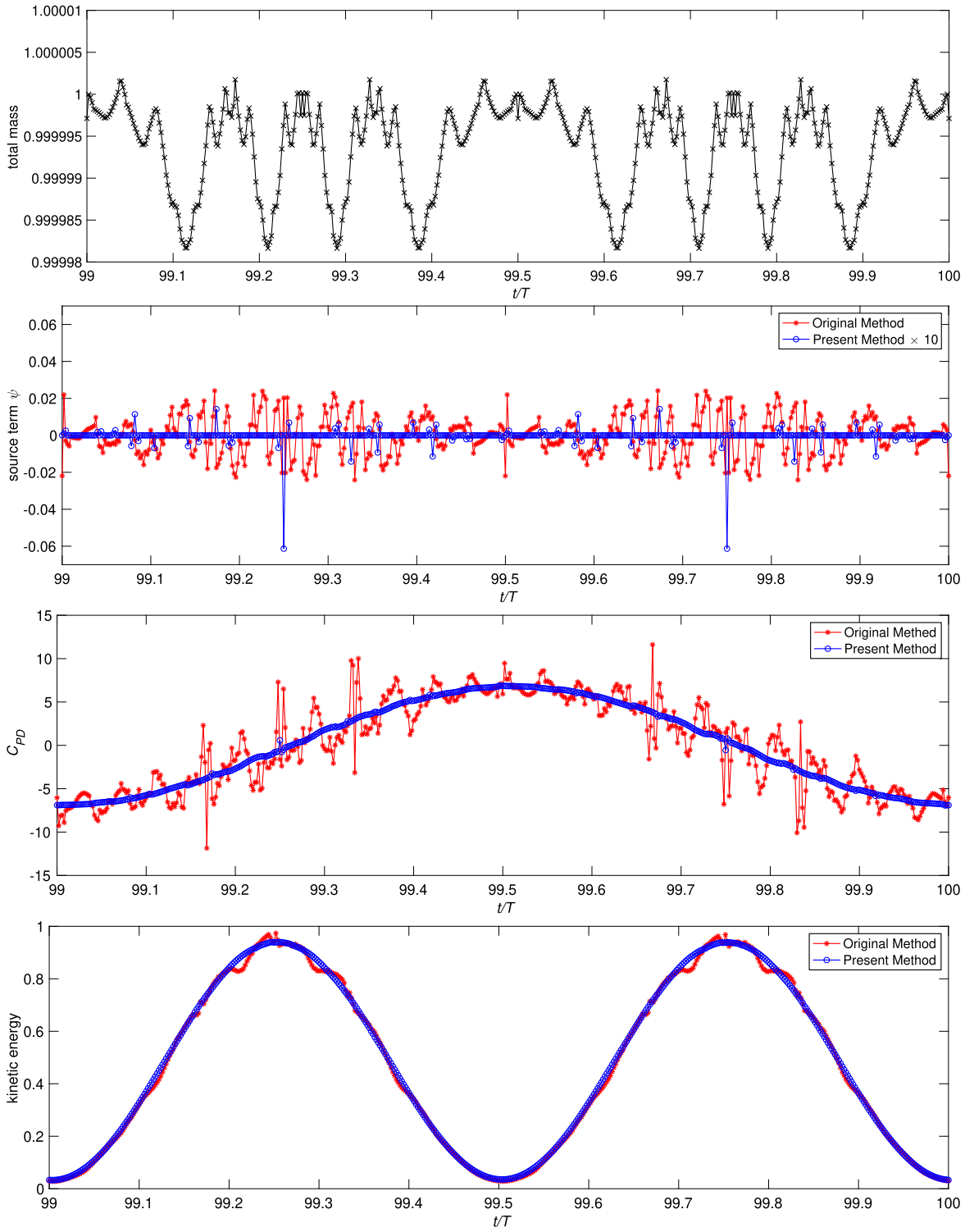

Fig. 7. Time histories of the total fluid mass conservation of the system, the integration of source term ψ for the whole domain, the pressure drag coefficient C_{PD} and the normalised kinetic energy for the horizontally oscillating circular cylinder at every time steps in one period for the 64×64 mesh: comparison between the original moving body algorithm [35] and the present moving body algorithm (Eq. (11)). The plot for the source term predicted by the present method is increased by 10 times for comparison.

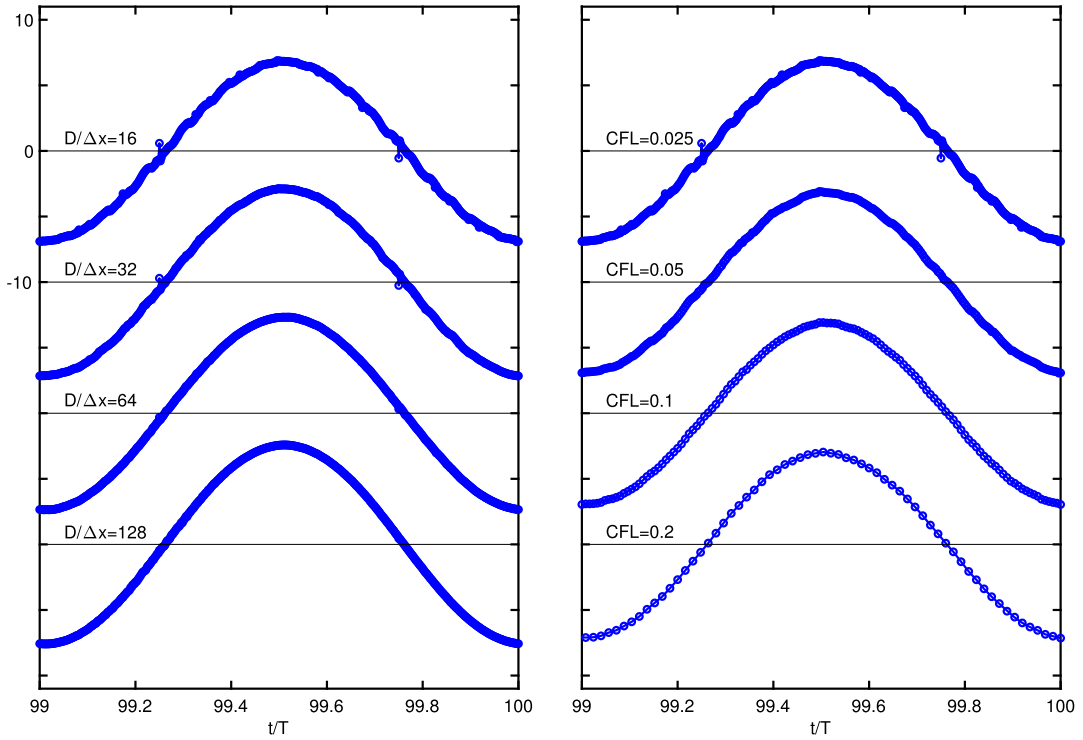

(a) mesh size (b) time step

Fig. 8. Time histories of the pressure drag coefficient C_{PD} for the horizontally oscillating circular cylinder with $X_0 = 0.125D$, $Re = 78.5$, $St = 1.27$. (a) The effect of mesh size with a fixed time step $\Delta t/T = 0.002$ and (b) the effect of time step on a fixed mesh resolution $D/\Delta x = 16$.

Fig. 10 shows the computed evolution of drag coefficient C_D, which includes the in-line force acting on the cylinder due to pressure and shear stress, and its comparison with the numerical result obtained from the boundary-fitted simulation [44]. A smooth force is predicted by the present method and it is in good agreement with the boundary-fitted result. This test demonstrates that the improved Cartesian cut-cell method not only reduces the spurious pressure oscillations, but can also predict accurately the flow field around the moving geometries.

4.4. Flow past a transversely oscillating circular cylinder

It is more complicated during fluid-structure interaction when the body moves in an established flow field. In the present study, the flow over a transversely oscillating cylinder is considered, which has been used as a benchmark case for different numerical methods, such as boundary-fitted [1,2], immersed boundary [11,13,14,45], and Cartesian cut-cell [23] methods. The computational setup is shown in Fig. 11, where a cylinder is oscillating vertically ($y_c(t) = y_c(0) - Y_0 \sin(2\pi f_e t)$) in a fluid with a free-stream velocity U_∞. The same parameters in previous studies are used here, in which the Reynolds number $Re = U_\infty D/\nu = 185$, the oscillation amplitude $Y_0 = 0.2D$, and the excitation frequency $f_e = 0.8 f_0$, where f_0 is the natural shedding frequency. The size of the computational domain is $[-20D, 40D] \times [-20D, 20D]$, with inflow velocity U_∞ at the inlet, zero gradient boundary condition at the outlet, and free slip boundary conditions at the top and bottom of the domain. Two non-uniform grids (600×528 and 1200×1056) are used for the spatial discretisation with uniform meshes $h = \Delta x_{\min} = \Delta y_{\min}$ ($h/D = 1/64, 1/128$) in the vicinity of the cylinder. Two constant CFL numbers (0.2 and 0.5) are used in the simulation.

Before considering the moving cylinder, we first study the flow over a stationary cylinder at the same Reynolds number. The time history of the computed drag (C_D) and lift (C_L) coefficients with the mesh resolution $h/D = 1/64$ and $CFL = 0.5$ is shown in Fig. 12, demonstrating the present method predicts smooth force acting on the cylinder and periodic vortex shedding can be observed for the flow. The time-averaged drag coefficient, the RMS-averaged lift coefficient, and the resulting Strouhal number are presented in Table 3. The results reported previously in the literature are also included for comparison, including those obtained from the experiment, body-fitted, different kinds of immersed boundary methods. For completeness, the sizes of the computational domain and mesh resolution are also summarised in Table 3. It can be seen that the present results obtained from the two sets of meshes and CFL numbers are in good agreement with those results obtained from previous numerical methods and experimentally measured values, which demonstrate the accuracy of the present cut-cell method to simulate the vortex shedding for flow over a circular cylinder.

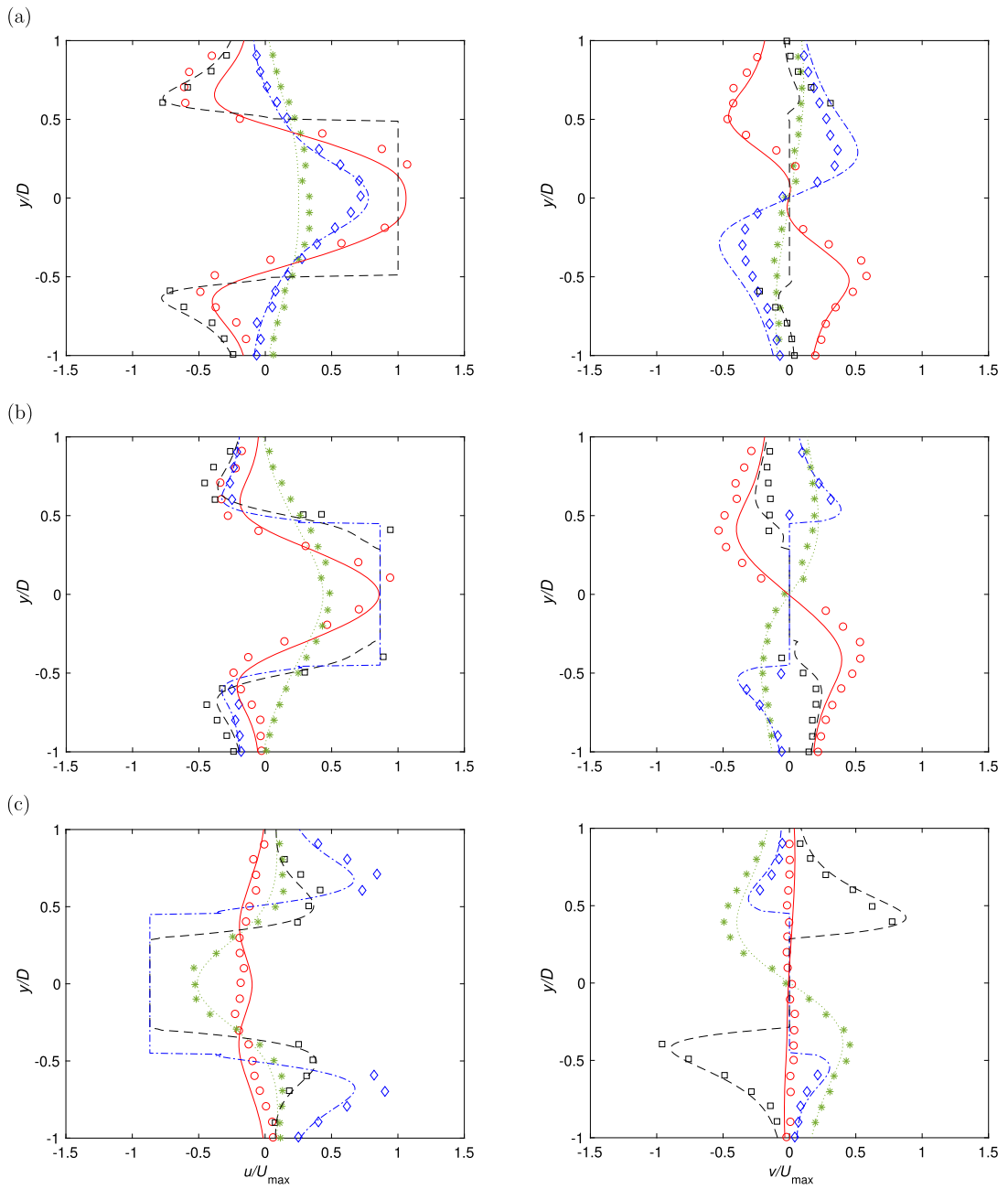

Fig. 9. Velocity profiles for in-line oscillating cylinder in a fluid at rest with $Re = 100$ and $KC = 5$ at (a) 180°; (b) 210°; (c) 330°. Lines are the present results and symbols are the experimental data [44] at four different locations: $x = -0.6D$ (red); $x = 0.0D$ (black); $x = 0.6D$ (blue); $x = 1.2D$ (green).

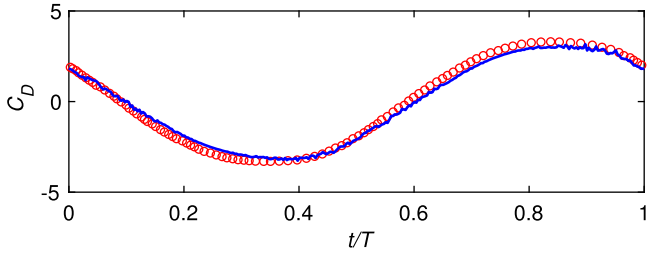

Fig. 10. Time history of the total drag coefficient C_D for in-line oscillating cylinder in a fluid at rest with $Re = 100$ and $KC = 5$. Solid line is the present result and circles are numerical results obtained by the boundary-fitted simulation [44].

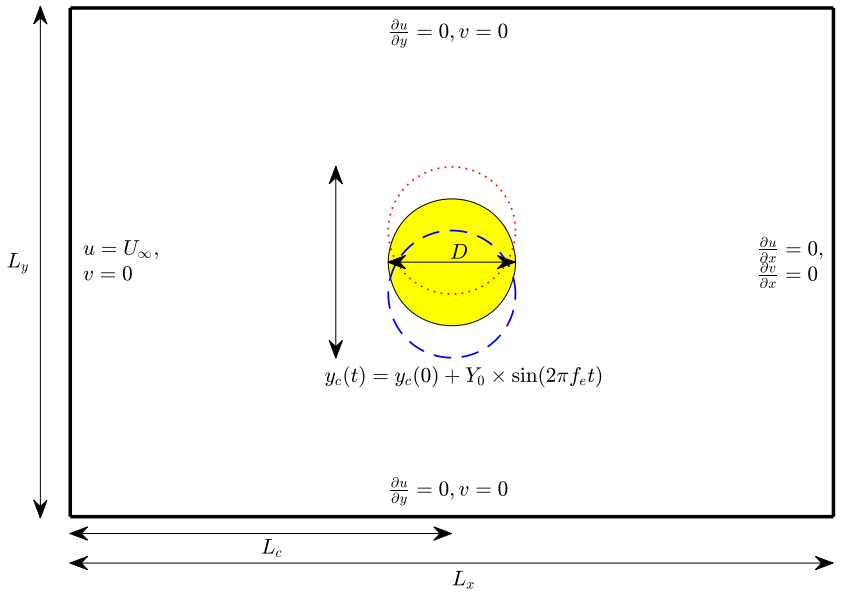

Fig. 11. Schematic of the computational setup for the flow past a transversely oscillating cylinder, in which a circular cylinder of diameter D is oscillating vertically in fluid with the free-stream velocity U_∞ in a domain $L_x \times L_y$ with zero gradient boundary condition for the outlet and free slip boundary conditions for both sides.

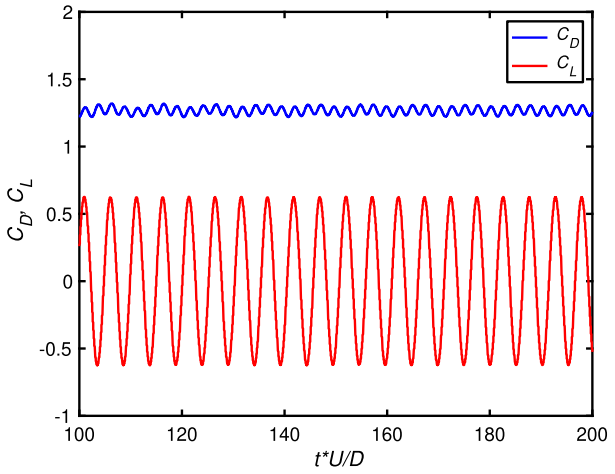

Fig. 12. Computed temporal variation of drag and lift coefficients for the flow over a stationary cylinder at $Re = 185$ with the mesh resolution $h/D = 1/64$ and $CFL = 0.5$.

Table 3
Comparison between experiment, boundary-fitted simulations, immersed boundary methods, and the present study for flow past a fixed cylinder at $Re = 185$.

Fixed cylinder at $Re = 185$	Method	D/h	$\bar{C}_D$	C_L^{rms}	St
Lu and Dalton [1]	experiment	–	1.28	–	0.19
Lu and Dalton [1]	boundary-fitted	–	1.31	0.422	0.195
Guilmineau and Queutey [2]	boundary-fitted	100	1.287	0.443	0.195
Yang and Balaras [14]	IBM-sharp interface	200	1.366	0.461	0.197
Abdol Azis et al. [45]	IBM-diffuse interface	60	1.362	–	0.193
Present study $CFL = 0.5$	cut-cell	64	1.267	0.440	0.195
Present study $CFL = 0.2$	cut-cell	64	1.319	0.436	0.195
Present study $CFL = 0.5$	cut-cell	128	1.335	0.451	0.195
Present study $CFL = 0.2$	cut-cell	128	1.335	0.448	0.195

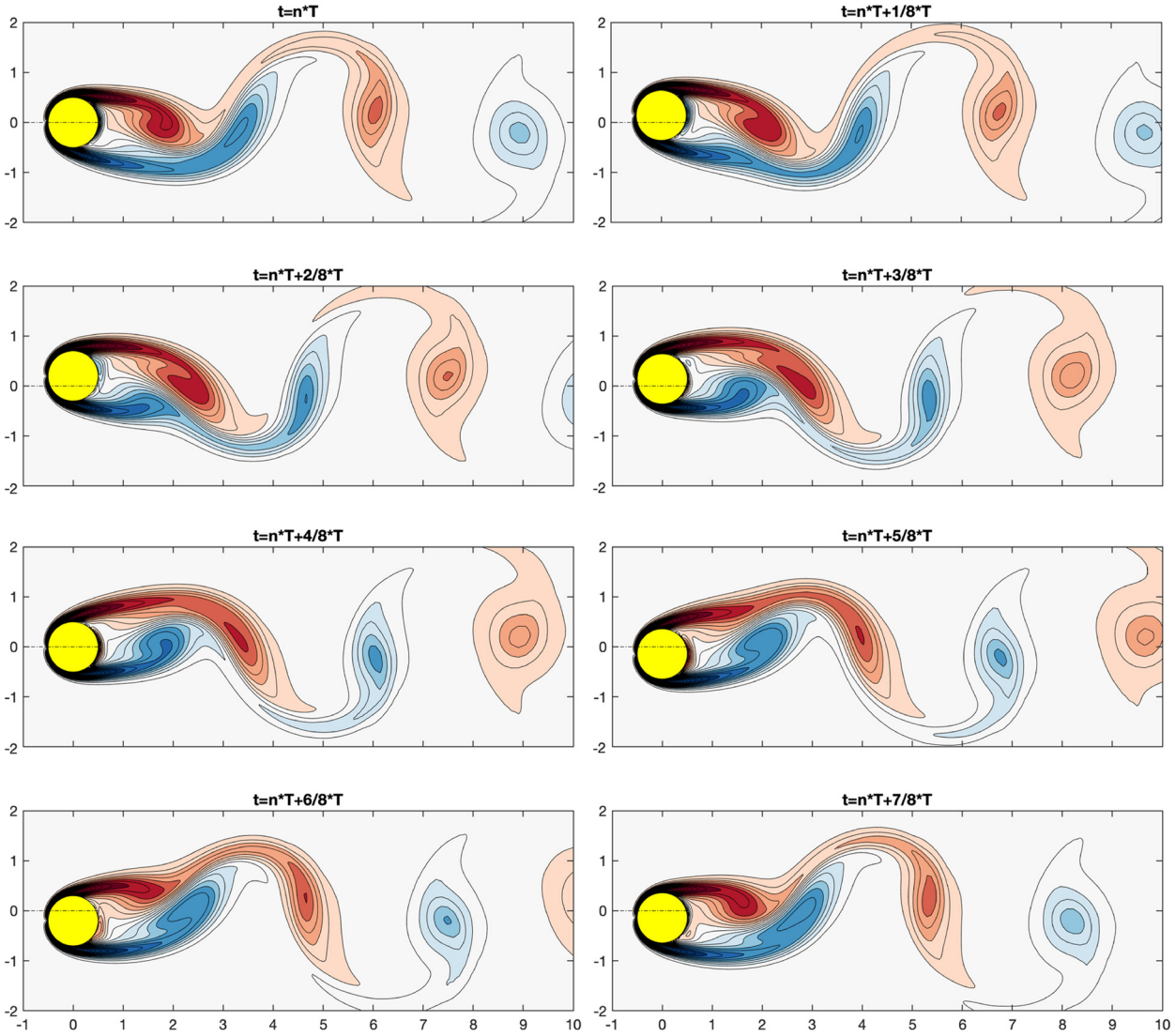

Fig. 13. The instantaneous vorticity fields in the wake of the flow over a transversely oscillating cylinder at $Re = 185$ with the mesh resolution $h/D = 1/64$ and $CFL = 0.5$. One oscillation period T is shown here with $1/8T$ interval between each snapshot.

Fig. 13 shows some snapshots of the vorticity contours for one oscillation period with $1/8T$ interval using the grid $h/D = 1/64$ and $CFL = 0.5$. Clockwise and anti-clockwise vortices are generated from the top and the bottom of the cylinder, respectively. The size and location of the vortex are similar for snapshots with $T/2$ interval, but with a different sign. It can be seen that periodic vortex shedding is observed from the cylinder and synchronises with the cylinder's forced oscillatory motion. The 2S mode can be seen in the wake of the cylinder, which is often observed in vortex-induced vibration problems.

Fig. 14 shows the variation of the drag and lift coefficients as a function of the cylinder's vertical position. It can be seen that relatively smooth hydrodynamic forces are obtained by the present cut-cell method and the amplitude of the oscillation decreases further when the mesh is refined. It is worth mentioning that in the immersed boundary method, large force oscillation is often observed when using the discrete delta function, where the spurious oscillation decreases when using the smooth delta function [11,13,45]. In the Cartesian cut-cell method, there is also spurious oscillation when using the cell-merging technique [23] and [23] proposed a weighting function together with the cut-cell method to reduce the spurious oscillation, which effectively smoothes the discretisation operator. However in the present method, there is no smoothing function used in the discretisation, and the reduced spurious oscillation is achieved by satisfying the continuity equation more accurately through the conservative and consistent cut-cell approach.

In order to make a quantitative validation, Table 4 shows the time-averaged drag coefficient, the RMS-averaged drag and lift coefficients, and the results reported previously in the literature, including those obtained from the body-fitted, different kinds of immersed boundary methods and Cartesian cut-cell methods. It can be seen that the present results obtained from

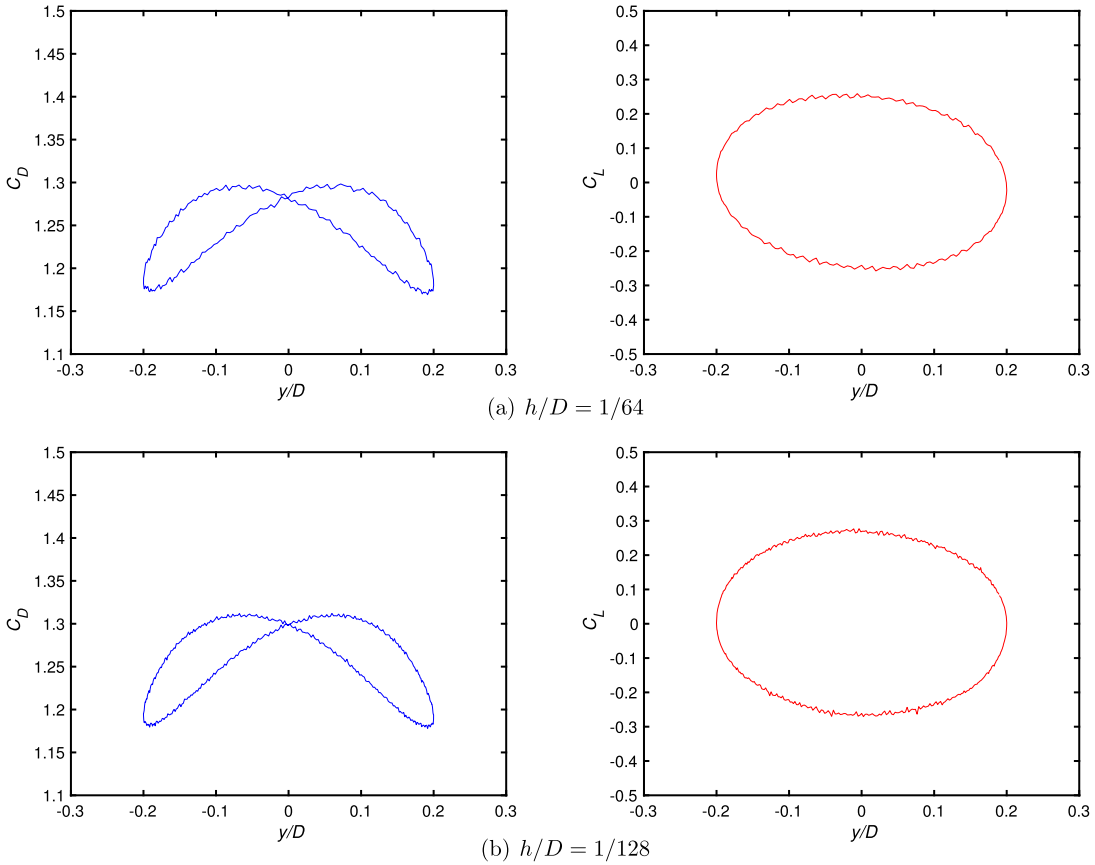

Fig. 14. Time-periodic variation of drag (C_D) and lift (C_L) coefficients as a function of the cylinder's vertical position for the flow over a transversely oscillating cylinder at $Re = 185$ using (a) 600×528 and (b) 1200×1056 grids with $CFL = 0.5$.

Table 4
Comparison between boundary-fitted simulations, immersed boundary methods, cut-cell method and the present study for flow past a transversely oscillating cylinder at $Re = 185$.

Oscillating at $Re = 185$	Method	D/h	$\bar{C}_D$	C_D^{rms}	C_L^{rms}
Lu and Dalton [1]	boundary-fitted	–	1.25	–	0.18
Guilmineau and Queutey [2]	boundary-fitted	100	1.195	0.036	0.08
Yang and Balaras [14]	IBM-sharp interface	200	1.21	0.040	0.08
Yang et al. [13]	IBM-sharp interface	100	1.281	0.042	0.076
Uhlmann [11]	IBM-diffuse interface	38.4	1.380	0.063	0.176
Abdol Azis et al. [45]	IBM-diffuse interface	60	1.260	0.059	0.0716
Schneiders et al. [23]	cut-cell (cell-merging)	50	1.259	0.040	0.059
Schneiders et al. [23]	cut-cell (weighting function)	50	1.279	0.042	0.082
Present study	cut-cell	64	1.234	0.043	0.180
Present study	cut-cell	128	1.246	0.047	0.190

the two sets of meshes are in good agreement with those results obtained from previous numerical methods, especially with the boundary-fitted simulation [1], which demonstrate the accuracy of the present cut-cell method to simulate the vortex-induced vibration problems.

4.5. An in-line oscillating sphere

After successfully simulating several 2D moving geometries, a canonical 3D problem for an oscillating sphere in the x direction [9,18] is considered here. The relevant parameters are: the oscillation amplitude $X_0 = 0.125D$, $Re = 78.54$ and $St = 1.2732$. The computational domain size is $(4D)^3$ and is discretised by a 64^3 uniform grid. Zero gradient boundary condition is applied in the x direction whereas no-slip boundary conditions are employed at all other boundaries. In the present cut-cell simulation, the sphere is resolved by 16 grid points ($h/D = 1/16$) and $CFL = 0.125$ is used in the simulation.

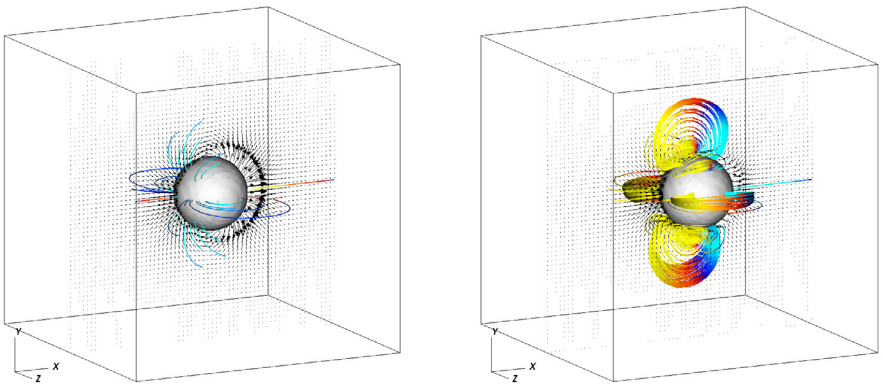

(a) $t = n * T + 1/4 * T$ (b) $t = n * T + 1/2 * T$

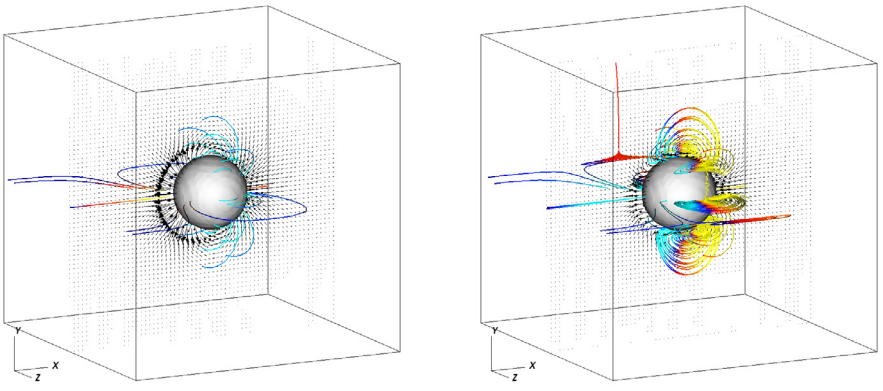

(c) $t = n * T + 3/4 * T$ (d) $t = n * T + T$

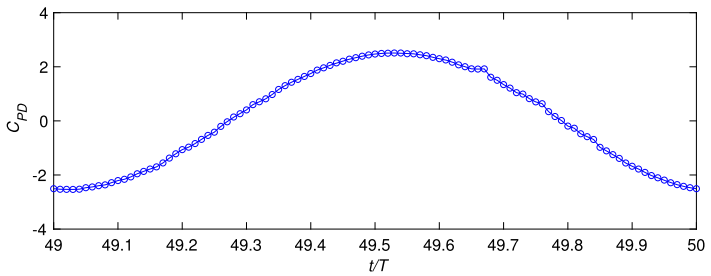

(e) pressure drag coefficient

Fig. 15. In-line oscillating sphere at $Re = 78.54$ and $St = 1.2732$. (a-d) instantaneous velocity vectors together with streamlines coloured by the pressure; (e) time history of the pressure drag coefficient plotted for every time step.

Fig. 15(a-d) shows the snapshots with $T/4$ time interval for the instantaneous velocity vectors together with streamlines coloured by the pressure. It can be seen that maximum velocity is obtained when the sphere moves across the centre at Fig. 15(a) and (c). Complicated flow structure can be observed when the sphere achieves its maximum oscillation position at Fig. 15(b) and (d), just before changing its moving direction.

Fig. 15(e) shows the time history of the pressure drag coefficient, at every time step during one oscillation period. Although relatively coarse mesh resolution is used to resolve the sphere, a very smooth drag coefficient is obtained, demonstrating the capability of the proposed sharp-interface cut-cell method in reducing spurious pressure oscillations in 3D.

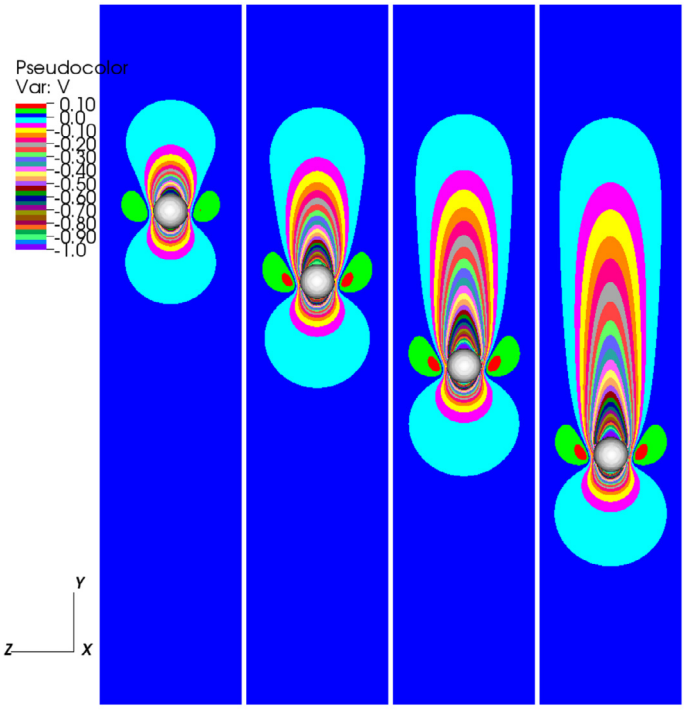

(a) velocity contours in a 2D plane

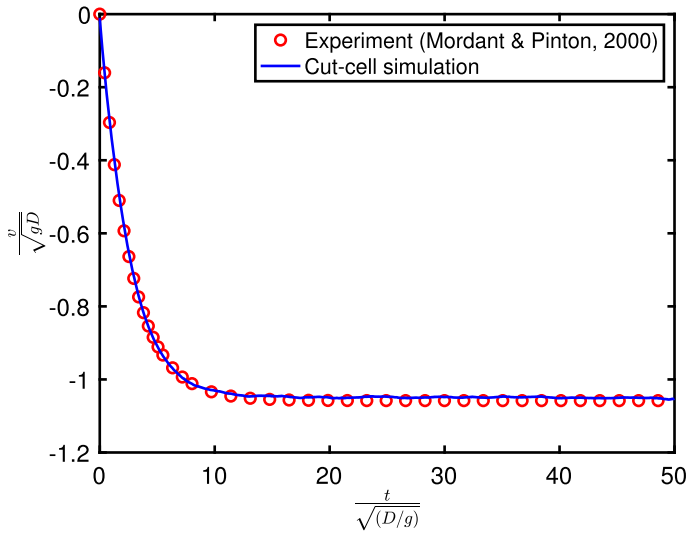

(b) settling velocity

Fig. 16. A single free-falling sphere in a fluid at rest with density ratio 2.56 and $Re = 41$: (a) snapshots for the contours of the vertical velocity during falling process; (b) predicted settling velocity compared with the experimental measurement [46].

4.6. A single free-falling sphere

In the final example, we consider a fluid-structure interaction problem for the motion of a solid sphere falling under the gravity in a fluid at rest, which has been studied previously by experimental [46] and numerical [11,47] approaches. The relevant parameters are chosen to match case 1 in the experiment [46], in which the density ratio between the sphere and the fluid is 2.56, Reynolds number and the Froude number based on the terminal velocity and the diameter of the sphere are $Re = 41$ and $Fr = 1.06$. The computational domain size is $[0, 8D] \times [0, 60D] \times [0, 8D]$ and is discretised by a

$128 \times 960 \times 128$ uniform grid. Zero gradient boundary condition is applied at the top and bottom of the domain in the y direction whereas free slip boundary conditions are employed at all other boundaries. The sphere is resolved by 16 grid points ($h/D = 1/16$) and the initial position for the sphere is at $(4D, 55D, 4D)$.

Fig. 16(a) shows some snapshots of the contours of the vertical velocity in a 2D plane during the initial stage of the free-falling sphere. It can be seen that the flow field is almost symmetric along the y axis and there is no axisymmetric vortex shedding due to the low Reynolds number. The sphere pushes the fluid downwards and also drags the fluid on its top to move down. There is a recirculation region on the side of the sphere, where the fluid is moving upwards. The wake region becomes longer until the sphere achieves its terminating velocity. In order the make a quantitative comparison, the predicted time history of the settling velocity is compared with the experimental data [46], where the velocity and time are normalised by $\sqrt{gD}$ and $\sqrt{(D/g)}$, respectively. A very good agreement is obtained for the present cut-cell method, demonstrating its capability in accurately predicting the hydrodynamic forces and movement in fluid-structure interaction problems.

5. Conclusions

A novel three-dimensional Cartesian cut-cell method has been developed for the simulation of moving complex geometries. Strict conservation of mass and momentum is enforced through the cut-cell method, together with a consistent mass and momentum flux. In contrary to existing cut-cell methods, an implicit time stepping scheme is employed, which prevents numerical instability without any additional small-cell treatment.

In the present study, the source of spurious pressure oscillations in the Cartesian cut-cell framework is investigated further. Local mass conservation errors, which are associated with (i) dead and fresh cells and (ii) geometrical conservation in the vicinity of complex geometries, are properly addressed by the present cut-cell method. In addition, other sources for local mass conservation errors are also noticed as: (iii) representation of curved geometries and (v) temporal discontinuity of the solid volume change. Thus, a new moving body algorithm is proposed for the cut-cell method, which effectively considers the motion of moving geometries and enforces exact mass conservation in the discretised level for cut-cells.

The present cut-cell method is validated through several popular benchmark cases in both 2D and 3D, in which the predicted results are compared with experimental measurements, boundary-fitted, various immersed boundary methods, and other cut-cell methods, with a close agreement being obtained with data reported in the literature. The temporal variations of pressure drag coefficients are shown for every time step in the simulations and it can be seen that pressure oscillations are significantly reduced by the cut-cell method, without using any smoothing technique. The improvement for local mass and momentum conservation enables a better understanding of fluid-structure interaction and flow-induced vibration problems.

CRediT authorship contribution statement

Zhihua Xie: Conceptualization, Data curation, Funding acquisition, Investigation, Methodology, Software, Validation, Visualization, Writing – original draft. **Pengzhi Lin:** Funding acquisition, Investigation, Methodology, Visualization, Writing – review & editing. **Thorsten Stoesser:** Funding acquisition, Investigation, Writing – review & editing.

Declaration of competing interest

The authors declare that they have no known competing financial interests or personal relationships that could have appeared to influence the work reported in this paper.

Acknowledgements

This work was financially supported by the Engineering and Physical Sciences Research Council (EPSRC) through grants (EP/R022135/1, EP/S016376/1, and EP/V040235/1), the Royal Society Newton Advanced Fellowship (NAF/R1/201156) and International Exchanges Award (IES/R2/202095), the National Natural Science Foundation of China (grant number 52031002), and the Open Fund of the State Key Laboratory of Hydraulics and Mountain River Engineering at Sichuan University (SKHL1904). Constructive comments from two anonymous reviewers for the improvement of the manuscript are gratefully acknowledged.

References

[1] X.-Y. Lu, C. Dalton, Calculation of the timing of vortex formation from an oscillating cylinder, J. Fluids Struct. 10 (1996) 527–541.
[2] E. Guilmineau, P. Queutey, A numerical simulation of vortex shedding from an oscillating circular cylinder, J. Fluids Struct. 16 (2002) 773–794.
[3] Z. Cheng, J. Li, C.Y. Loh, L.-S. Luo, An exactly force-balanced boundary-conforming arbitrary-Lagrangian-Eulerian method for interfacial dynamics, J. Comput. Phys. 408 (2020) 109237.
[4] F. Sotiropoulos, X. Yang, Immersed boundary methods for simulating fluid–structure interaction, Prog. Aerosp. Sci. 65 (2014) 1–21.
[5] S. Roy, A. De, E. Balaras, Immersed Boundary Method: Development and Applications, Springer, Singapore, 2020.
[6] R. Mittal, G. Iaccarino, Immersed boundary methods, Annu. Rev. Fluid Mech. 37 (2005) 239–261.

[7] B.E. Griffith, N.A. Patankar, Immersed methods for fluid–structure interaction, Annu. Rev. Fluid Mech. 52 (2020) 421–448.
[8] D.M. Ingram, D.M. Causon, C.G. Mingham, Developments in Cartesian cut cell methods, Math. Comput. Simul. 61 (2003) 561–572.
[9] J.H. Seo, R. Mittal, A sharp-interface immersed boundary method with improved mass conservation and reduced spurious pressure oscillations, J. Comput. Phys. 230 (2011) 7347–7363.
[10] H. Luo, H. Dai, P.J. Ferreira de Sousa, B. Yin, On the numerical oscillation of the direct-forcing immersed-boundary method for moving boundaries, Comput. Fluids 56 (2012) 61–76.
[11] M. Uhlmann, An immersed boundary method with direct forcing for the simulation of particulate flows, J. Comput. Phys. 209 (2005) 448–476.
[12] K. Taira, T. Colonius, The immersed boundary method: a projection approach, J. Comput. Phys. 225 (2007) 2118–2137.
[13] X. Yang, X. Zhang, Z. Li, G.-W. He, A smoothing technique for discrete delta functions with application to immersed boundary method in moving boundary simulations, J. Comput. Phys. 228 (2009) 7821–7836.
[14] J. Yang, E. Balaras, An embedded-boundary formulation for large-eddy simulation of turbulent flows interacting with moving boundaries, J. Comput. Phys. 215 (2006) 12–40.
[15] J. Kim, D. Kim, H. Choi, An immersed-boundary finite-volume method for simulations of flow in complex geometries, J. Comput. Phys. 171 (2001) 132–150.
[16] D. Kim, H. Choi, Immersed boundary method for flow around an arbitrarily moving body, J. Comput. Phys. 212 (2006) 662–680.
[17] J. Lee, J. Kim, H. Choi, K.-S. Yang, Sources of spurious force oscillations from an immersed boundary method for moving-body problems, J. Comput. Phys. 230 (2011) 2677–2695.
[18] J. Lee, D. You, An implicit ghost-cell immersed boundary method for simulations of moving body problems with control of spurious force oscillations, J. Comput. Phys. 233 (2013) 295–314.
[19] M. Kumar, S. Roy, A sharp interface immersed boundary method for moving geometries with mass conservation and smooth pressure variation, Comput. Fluids 137 (2016) 15–35.
[20] H.S. Udaykumar, W. Shyy, M.M. Rao, ELAFINT: a mixed Eulerian-Lagrangian method for fluid flows with complex and moving boundaries, Int. J. Numer. Methods Fluids 22 (1996) 691–712.
[21] W.P. Bennett, N. Nikiforakis, R. Klein, A moving boundary flux stabilization method for Cartesian cut-cell grids using directional operator splitting, J. Comput. Phys. 368 (2018) 333–358.
[22] M. Meinke, L. Schneiders, C. Gunther, W. Schroder, A cut-cell method for sharp moving boundaries in Cartesian grids, Comput. Fluids 85 (2013) 135–142.
[23] L. Schneiders, D. Hartmann, M. Meinke, W. Schroder, An accurate moving boundary formulation in cut-cell methods, J. Comput. Phys. 235 (2013) 786–809.
[24] G. Dechriste, L. Mieussens, A Cartesian cut cell method for rarefied flow simulations around moving obstacles, J. Comput. Phys. 314 (2016) 465–488.
[25] B. Muralidharan, S. Menon, Simulation of moving boundaries interacting with compressible reacting flows using a second-order adaptive Cartesian cut-cell method, J. Comput. Phys. 357 (2018) 230–262.
[26] H.S. Udaykumar, H.C. Kan, W. Shyy, R. Tran-Son-Tay, Multiphase dynamics in arbitrary geometries on fixed Cartesian grids, J. Comput. Phys. 137 (1997) 366–405.
[27] K.M.T. Kleefsman, G. Fekken, A.E.P. Veldman, B. Iwanowski, B. Buchner, A volume-of-fluid based simulation method for wave impact problems, J. Comput. Phys. 206 (2005) 363–393.
[28] L. Qian, D.M. Causon, C.G. Mingham, D.M. Ingram, A free-surface capturing method for two fluid flows with moving bodies, Proc. R. Soc. A, Math. Phys. Eng. Sci. 462 (2006) 21–42.
[29] M.H. Chung, An adaptive Cartesian cut-cell/level-set method to simulate incompressible two-phase flows with embedded moving solid boundaries, Comput. Fluids 71 (2013) 469–486.
[30] Z. Xie, T. Stoesser, S. Yan, Q. Ma, P. Lin, A Cartesian cut-cell based multiphase flow model for large-eddy simulation of three-dimensional wave-structure interaction, Comput. Fluids 213 (2020) 104747.
[31] Q. Chen, J. Zang, A.S. Dimakopoulos, D.M. Kelly, C.J.K. Williams, A Cartesian cut cell based two-way strong fluid-solid coupling algorithm for 2d floating bodies, J. Fluids Struct. 62 (2016) 252–271.
[32] L. Schneiders, C. Gunther, M. Meinke, W. Schroder, An efficient conservative cut-cell method for rigid bodies interacting with viscous compressible flows, J. Comput. Phys. 311 (2016) 62–86.
[33] V. Pasquariello, G. Hammerl, F. Örley, S. Hickel, C. Danowski, A. Popp, W.A. Wall, N.A. Adams, A cut-cell finite volume – finite element coupling approach for fluid–structure interaction in compressible flow, J. Comput. Phys. 307 (2016) 670–695.
[34] D.M. Causon, D.M. Ingram, C.G. Mingham, G. Yang, R.V. Pearson, Calculation of shallow water flows using a Cartesian cut cell approach, Adv. Water Resour. 23 (2000) 545–562.
[35] Z. Xie, T. Stoesser, A three-dimensional Cartesian cut-cell/volume-of-fluid method for two-phase flows with moving bodies, J. Comput. Phys. 416 (2020) 109536.
[36] P. Lin, A fixed-grid model for simulation of a moving body in free surface flows, Comput. Fluids 36 (2007) 549–561.
[37] Z. Xie, Numerical study of breaking waves by a two-phase flow model, Int. J. Numer. Methods Fluids 70 (2012) 246–268.
[38] Z. Xie, A two-phase flow model for three-dimensional breaking waves over complex topography, Proc. R. Soc. A, Math. Phys. Eng. Sci. 471 (2015) 20150101.
[39] R.I. Issa, Solution of the implicitly discretised fluid flow equations by operator-splitting, J. Comput. Phys. 62 (1986) 40–65.
[40] H.A. van der Vorst, Bi-CGSTAB - a fast and smoothly converging variant of Bi-CG for the solution of nonsymmetric linear-systems, SIAM J. Sci. Stat. Comput. 13 (1992) 631–644.
[41] A. Sohankar, C. Norberg, L. Davidson, Low-Reynolds-number flow around a square cylinder at incidence: study of blockage, onset of vortex shedding and outlet boundary condition, Int. J. Numer. Methods Fluids 26 (1998) 39–56.
[42] S. Sen, S. Mittal, G. Biswas, Flow past a square cylinder at low Reynolds numbers, Int. J. Numer. Methods Fluids 67 (2011) 1160–1174.
[43] S. Ryu, G. Iaccarino, Vortex-induced rotations of a rigid square cylinder at low Reynolds numbers, J. Fluid Mech. 813 (2017) 482–507.
[44] H. Dutsch, F. Durst, S. Becker, H. Lienhart, Low-Reynolds-number flow around an oscillating circular cylinder at low Keulegan–Carpenter numbers, J. Fluid Mech. 360 (1998) 249–271.
[45] M.H. Abdol Azis, F. Evrard, B. van Wachem, An immersed boundary method for incompressible flows in complex domains, J. Comput. Phys. 378 (2019) 770–795.
[46] N. Mordant, J. Pinton, Velocity measurement of a settling sphere, Eur. Phys. J. B 18 (2000) 343–352.
[47] N. Sharma, N.A. Patankar, A fast computation technique for the direct numerical simulation of rigid particulate flows, J. Comput. Phys. 205 (2005) 439–457.